

Nonlinear Radiating Instability of a Barotropic Eastern Boundary Current

JINBO WANG

Massachusetts Institute of Technology/WHOI Joint Program, Cambridge, Massachusetts

MICHAEL A. SPALL

Woods Hole Oceanographic Institution, Woods Hole, Massachusetts

GLENN R. FLIERL AND PAOLA MALANOTTE-RIZZOLI

Massachusetts Institute of Technology, Cambridge, Massachusetts

(Manuscript received 11 September 2012, in final form 24 March 2013)

ABSTRACT

Linear and nonlinear radiating instabilities of an eastern boundary current are studied using a barotropic quasigeostrophic model in an idealized meridional channel. The eastern boundary current is meridionally uniform and produces unstable modes in which long waves are most able to radiate. These long radiating modes are easily suppressed by friction because of their small growth rates. However, the long radiating modes can overcome friction by nonlinear energy input transferred from the more unstable trapped mode and play an important role in the energy budget of the boundary current system. The nonlinearly powered long radiating modes take away part of the perturbation energy from the instability origin to the ocean interior. The radiated instabilities can generate zonal striations in the ocean interior that are comparable to features observed in the ocean. Subharmonic instability is identified to be responsible for the nonlinear resonance between the radiating and trapped modes, but more general nonlinear triad interactions are expected to apply in a highly nonlinear environment.

1. Introduction

Energetic mesoscale variability in the ocean interior has long been observed (Wyrtki et al. 1976; Stammer 1997) and motivated many studies concerning its origins. The most direct mechanism is baroclinic instability of the large-scale circulation. Gill et al. (1974) noted that the potential energy of large-scale wind-driven gyres in the ocean is several orders of magnitude larger than their kinetic energy. The vast stores of potential energy might be released through baroclinic instability to generate mesoscale eddies much stronger than the mean circulation (Gill et al. 1974; Robinson and McWilliams 1974). Although theory suggests that the eddy energy in weakly sheared zonal flows is limited by the shear of the mean flow (Pedlosky 1975), an introduction of a meridional component to the mean flow allows for eddy

kinetic energy exceeding that of the mean (Robinson and McWilliams 1974; Spall 2000).

An alternative mechanism is related to the radiation of mechanical energy from swift oceanic boundary currents, such as the Gulf Stream. Many studies represent the Gulf Stream as a propagating northern boundary (Flierl and Kamenkovich 1975; Pedlosky 1977; Harrison and Robinson 1979; Malanotte-Rizzoli et al. 1987). These results identify important mechanisms governing the energy radiation from strong ocean currents. Talley (1983) derives the wave properties by solving for the stability of a steady zonal flow and shows that instability radiation will not occur unless there is a westward component in the zonal current or the far field is made baroclinic. The main argument is that the wave characteristics of eastward-traveling instabilities do not match the dispersion relation of the free Rossby waves in the far field.

Instability radiation occurs more easily for a nonzonal current. Pedlosky (1993) studied a baroclinic shear flow that is inclined with respect to a latitude circle. Although the study focuses on the generation of a boundary current

Corresponding author address: Jinbo Wang, 9500 Gilman Dr. #0230, La Jolla, CA 92093.
E-mail: jinbow@alum.mit.edu

by the boundary trapping of two reflected unstable waves, it clearly demonstrates that a nonzonal flow is less stable and its instabilities can reach out to the far region. Kamenkovich and Pedlosky (1996, 1998a,b) explicitly studied the influence of nonzonality on jet instability and radiation. They found that even a slight nonzonality in the mean flow can generate radiating instabilities, which can significantly penetrate into the far field.

A meridional current is an extreme case of the nonzonality. The instabilities generated by a meridional western boundary current are able to radiate eastward even in the presence of realistic dissipation (Fantini and Tung 1987). Hristova et al. (2008) studied the radiating instabilities of meridional boundary currents and compared a western boundary current with an eastern boundary current. They showed that an eastern boundary current supports a greater number of radiating modes over a wider range of meridional wavenumbers than a western boundary current. However, these studies used a piecewise constant meridional velocity profile. This velocity profile reduces the stability equation to an ordinary differential equation with constant coefficients, which is easier to solve, but leads to unrealistic shortwave behaviors. Wang et al. (2012) extended these previous studies by considering a continuous velocity profile in a barotropic quasigeostrophic model and demonstrated that radiating instabilities can generate zonal striations in the ocean interior. The nonlinear effects were shown to be important in energizing the instability radiation. As a follow-up study, we here discuss the mechanism that governs the nonlinear radiating instabilities of an eastern boundary current.

2. The model

We choose the simplest barotropic quasigeostrophic (QG) model, as used in Fantini and Tung (1987) and Wang et al. (2012), to focus on elementary nonlinear dynamics. The model is described by the barotropic vorticity equation:

$$\begin{aligned} \partial_t q + J(\psi, q) &= \mathcal{F} \quad \text{and} \\ q &= \nabla^2 \psi + \beta y, \end{aligned} \quad (1)$$

where ψ is streamfunction, q is potential vorticity, \mathcal{F} is an external forcing and friction, J is the Jacobian operator, and β is the meridional gradient of the Coriolis parameter.

In a linear or weakly nonlinear state, the total field can be decomposed into a basic steady state (denoted by the overbar) and perturbations (denoted by the prime),

$$\begin{aligned} \psi &= \bar{\psi} + \psi' \quad \text{and} \\ q &= \bar{q} + q' = \nabla^2 \bar{\psi} + \beta y + \nabla^2 \psi', \end{aligned} \quad (2)$$

where the perturbation field is much weaker than the basic state. The basic state is assumed to be balanced by a steady external forcing

$$\bar{\mathcal{F}} = J(\bar{\psi}, \bar{q}) \equiv -\bar{\psi}_y \nabla^2 \bar{\psi}_x + \bar{\psi}_x \nabla^2 \bar{\psi}_y + \beta \bar{\psi}_x, \quad (3)$$

where the subscripts denote partial derivatives. Here, $\bar{\psi}$ is not the time-mean streamfunction, and ψ' can have a mean part; when we require means, we will denote them specifically by a time integral. For a basic state with only a zonal flow, no external forcing is needed as $\bar{\psi}_x = 0$. However, an external forcing is necessary to maintain a basic meridional flow. It takes the form $\bar{\mathcal{F}} = \beta \bar{v}$, where $(\bar{u}, \bar{v}) = (-\bar{\psi}_y, \bar{\psi}_x)$ is the steady-state barotropic flow, meaning a vorticity source or sink is needed to compensate the planetary vorticity change caused by the meridional movement of a water parcel.

After substituting Eqs. (2) and (3), Eq. (1) becomes

$$\partial_t q' + J(\bar{\psi}, q') + J(\psi', \bar{q}) + J(\psi', q') = \mathcal{F}', \quad (4)$$

where \mathcal{F}' represents frictional effects on perturbations.

This equation is solved numerically to investigate the influence of nonlinearity on the instability of a meridional current. To study linear stability, the quadratic term in ψ' is neglected, resulting in the linear stability equation

$$\partial_t q' + J(\bar{\psi}, q') + J(\psi', \bar{q}) = \mathcal{F}'. \quad (5)$$

In the following sections, we first study the linear and then the nonlinear stability problem of an eastern boundary current by numerically solving Eqs. (5) and (4), respectively.

3. Linear radiating instability

a. Stability equation

Let us consider a basic state with a parallel meridional eastern boundary current $\bar{v}(x)$. We set $x = -L_x$ at the western boundary and $x = 0$ at the eastern boundary. The linear stability Eq. (5) can be nondimensionalized using the cross-stream length scale L_b and the velocity scale V of the boundary current. After dropping primes without causing confusion, the linearized Eq. (5) becomes

$$(\partial_t + \bar{v} \partial_y) \nabla^2 \psi + \beta^* \psi_x - \bar{v}_{xx} \psi_y - \mathcal{F}(\psi) = 0, \quad (6)$$

where $\beta^* = \beta L_b^2/V$ is the nondimensional beta, and $\mathcal{F}(\psi)$ is the frictional damping on perturbations, which can be specified as Laplacian diffusion of vorticity $\nabla \cdot A_H \nabla q$, where A_H is the horizontal viscosity. Nonzero A_H will be used in the nonlinear simulations, but here we first consider the inviscid problem as a first step in the study of nonlinear instability. A normal mode solution is assumed in y and t for perturbations,

$$\psi = \phi(x)e^{il(y-ct)} + \text{c.c.}, \quad (7)$$

where l is meridional wavenumber, c is meridional phase speed, and c.c. is the complex conjugate. Substituting Eq. (7) into (6) results in a Sturm–Liouville eigenvalue problem,

$$\phi_{xx} + \frac{\beta^*}{il(\bar{v} - c)} \phi_x - \left(l^2 + \frac{\bar{v}_{xx}}{\bar{v} - c} \right) \phi = 0. \quad (8)$$

This is the stability equation for an inviscid, barotropic, quasigeostrophic, meridional current. Previous studies, for example, Fantini and Tung (1987) and Hristova et al. (2008), further simplify it to an ordinary differential equation system by choosing a step function to represent the boundary current \bar{v} . The simplified stability equation becomes easier to solve, but there is no shortwave cutoff. The discontinuous velocity profile generates a delta function in the background vorticity and supports instabilities with infinitely large wavenumbers.

In this study, we use a continuous profile to represent the boundary current to aid the comparison between linear and nonlinear theories. The profile is similar to Wang et al. (2012):

$$\bar{v}(x) = -V \operatorname{sech}^2\left(\frac{x - x_0}{L_b}\right), \quad (9)$$

where x_0 is the location of the center of the boundary current.

Two methods are used to solve the linear problem with a continuous velocity $\bar{v}(x)$. The linear eigenvalue problem represented by Eq. (8) with proper boundary conditions discussed below is solved by a shooting method. The second method considers an initial value problem for both inviscid and viscous cases. The linear model equation in Eq. (6) is initialized with a sine wave, whose growth rates are calculated by fitting the time series of the square root of the domain-integrated energy to an exponential curve. The boundary conditions for the initial value problem are no-normal-flow at the eastern and western solid boundaries and periodic conditions in the meridional direction. The boundary conditions needed for the shooting method are discussed as follows.

b. Boundary conditions and radiating modes

The no-normal-flow boundary condition is applied at the solid eastern boundary,

$$\phi(0) = 0. \quad (10)$$

In the regions away from the boundary current, say $x = -L_i$, \bar{v} approaches zero, so that perturbation eigenfunctions satisfy the free Rossby wave dispersion relation and their zonal structures is proportional to e^{ikx} , where the zonal wavenumber k satisfies

$$k^2 + \frac{\beta^*}{lc} k + l^2 = 0. \quad (11)$$

The boundary condition at $x = -L_i$ is the radiation condition

$$\phi_x(-L_i) = ik\phi(-L_i), \quad (12)$$

where k is one of the two solutions of Eq. (11). It is chosen in such a way that it either represents a decay structure or an outward (westward in this case) propagation of wave energy. The two solutions of k , say $k^{(1)}$ and $k^{(2)}$, have opposite-signed imaginary parts since their product, $k^{(1)}k^{(2)} = l^2$ is real. The eigenfunction $\phi(x)$ of an eastern boundary current decays westward, requiring the imaginary part of k , that is, k_i , to be negative. Negative k_i also corresponds to westward Rossby wave group velocity in the limit of $c_i \rightarrow 0$ (Hristova et al. 2008).

Extra analysis is required to distinguish radiating modes from trapped modes, as they both decay into the far field. The decaying structure of an unstable radiating mode is formed because the packets of perturbations take finite time to propagate away into the interior with relatively unchanged amplitude, meanwhile grow exponentially near the energy source. The amplitude of an unstable radiating mode is always larger over the jet region than in the interior. A necessary condition used to identify a radiating mode is the so-called phase speed condition, that is, the dispersion relation of a radiating mode has to match the dispersion relation of the free waves in the interior, Rossby waves in this case (Talley 1983).

c. Results

Figure 1 shows the linear growth rate lc_i and frequency ω_r as a function of wavenumber l , where c_i and ω_r are the imaginary and real parts of c and $\omega = lc$, respectively. Note that there are two unstable modes for a sech^2 velocity profile on an f plane, which are a sinuous mode and a varicose mode, corresponding to symmetric and

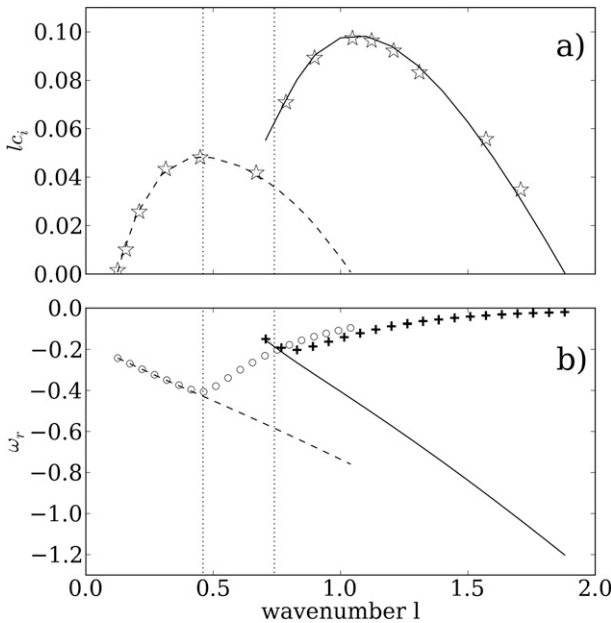


FIG. 1. (a) The growth rates calculated by a shooting method (lines) and an initial value method (stars) are shown. (b) The real frequencies calculated from eigenvalues, $\omega_r = lc_r$ (lines) and $\omega_r = -\beta^* k_r / (k_r^2 + l^2)$ (symbols) are shown. In (a),(b), the dashed lines represent modified varicose modes, and the solid lines represent modified sinuous modes. The two critical wave numbers separating the radiating and trapped modes are $l = 0.46$ for the modified varicose mode and $l = 0.74$ for the modified sinuous mode are marked by the two dotted vertical lines in Fig. 1b).

antisymmetric eigenfunction structures, respectively (Lipps 1962). In our case, the beta effect and side boundary effect alter the original eigenfunctions resulting in modified sinuous and varicose modes, which are indicated by the solid and dashed lines in Fig. 1.

Figure 1a shows that the most unstable mode is a sinuous mode (solid line) at $l = 1.05$. The modified sinuous mode has a shortwave cutoff at $l = 1.88$. No unstable sinuous modes are found for $l < 0.706$. Unstable modes over the longwave range are modified varicose modes (dashed line). Instabilities exist for $0.125 < l < 1.04$. The calculation by the initial value method for the inviscid case is shown by the stars. The good agreement between the lines and the symbols validates both methods. Frictional and nonlinear terms are added to the linear numerical model used in the initial value problem to study nonlinear effect in the next section.

Figure 1b shows the frequency ω_r . The lines indicate $\omega_r = lc_r$, while the symbols represent $\omega_r = -\beta k_r / (k_r^2 + l^2)$. According to the phase speed condition, the two frequencies at each l should be equal in order for instabilities to radiate. For the modified varicose mode (dashed line), the circles fall on the dashed line over the wavenumber range $l < 0.46$, meaning the longwave modes with $l < 0.46$ are expected to radiate. Similarly,

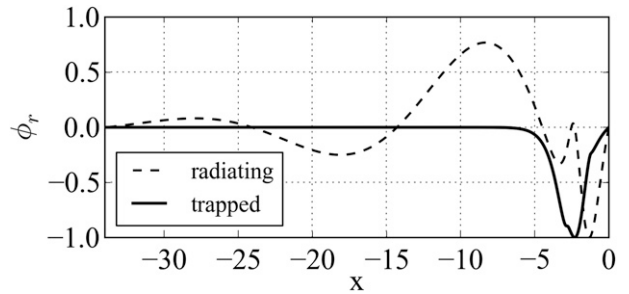


FIG. 2. The real part of the eigenfunctions of the radiating (dashed) and trapped (solid) modes as a function of x (x is normalized by L_b). The radiating mode has $l = 0.4$, $k = 0.21 - i0.0011$, and the trapped mode has $l = 0.82$, $k = 0.32 - i0.74$.

long sinuous modes (solid line) with $l < 0.74$ are also expected to radiate, but only over a very narrow wavenumber range $0.706 < l < 0.74$. The two critical wave numbers separating the radiating and trapped modes are $l = 0.46$ for the modified varicose mode and $l = 0.74$ for the modified sinuous mode (the two dotted vertical lines in Fig. 1b).

One example of the eigenfunctions for radiating mode and trapped mode are shown in Fig. 2. The eigenfunctions show a wavy structure for the radiating mode, but a fast-decay structure for the trapped mode.

The linear analysis shows that radiating instabilities occur over the longwave end for each mode (sinuous or varicose). It is qualitatively consistent with Kamenkovich and Pedlosky (1996) and Hristova et al. (2008). Although radiating modes are able to transfer energy away from the unstable region to affect the interior, they have smaller growth rates than the most unstable mode in this inviscid linear theory. Friction can suppress the unstable inviscid radiating modes, leaving the significance of the radiating mode in question.

4. Nonlinear radiating instability

The exponential growth of an initially infinitesimal perturbation slows down when the perturbation becomes finite and starts to feed back into the mean. Once an initial small perturbation develops to finite amplitude, linear theory fails and nonlinear interaction becomes important for the perturbation development. The elementary mechanism for nonlinear interaction is the triad resonance, which describes that a triad of waves are resonant if their phases satisfy $\theta_1 \pm \theta_2 \pm \theta_3 = 0$, which is equivalent to both wavenumbers and frequencies satisfying $l_1 \pm l_2 \pm l_3 = 0$ and $\omega_1 \pm \omega_2 \pm \omega_3 = 0$ (Phillips 1960). Here we are interested in identifying the effect of nonlinear interaction on the radiating instabilities from the point of view of elementary triad resonance. To

single out the nonlinear process among a wave triad, we weakly force the model to generate only one linearly unstable mode (denoted as the primary mode henceforth), suppress other modes by friction, and look for a wave triad that is resonant. A case with a nonresonant wave triad is presented in section 4d as a comparison.

The model is described by Eq. (4), where the damping is provided by Laplacian diffusion of vorticity $\mathcal{F} = \nabla \cdot A_H \nabla q$ (after dropping primes). Here, A_H is strongly increased at the western boundary to remove energy and enstrophy as used in Fox-Kemper (2003):

$$A_H = A_H^w - (A_H^w - A_H^e) \exp\left(\frac{x}{\alpha L_x}\right), \quad (13)$$

where α controls the decay scale. This function changes from approximately A_H^w at the western boundary to A_H^e at the eastern boundary. Different values of α are tested to confirm that our conclusions are not sensitive to α as long as A_H is approximately A_H^e over the eastern boundary current region. The frictional effect in the interior is not energetically important as the perturbation field has a large horizontal scale (see the appendix for the scaling argument). Bottom friction was also tested to confirm that our conclusion about the nonlinear interaction between trapped and radiating modes does not depend on the specific form of friction (not shown). Cases with $\alpha = 0.15$ are presented here. We use $A_H^w = 10^4 \text{ m}^2 \text{ s}^{-1}$ and $A_H^e = 100 \text{ m}^2 \text{ s}^{-1}$ in this study. The perturbation energy budget over the eastern boundary current region varies for different values of A_H^e .

The model domain is an $L_x \times L_y$ meridional channel discretized using $N_x \times N_y$ grid points, which are specified in each following section. The boundary conditions are periodic in the meridional direction, with no-normal-flow and slip conditions along the solid walls.

The velocity profile is described by Eq. (9) with $V = 0.11 \text{ m s}^{-1}$, $L_b = 50 \text{ km}$, and $x_0 = -100 \text{ km}$. The speed [$\mathcal{O}(10 \text{ cm s}^{-1})$] and the width of the boundary current are consistent with observations (Hickey 1979; Davis 1985; Brink and Cowles 1991). Other velocity profiles were also tested without altering our final conclusions.

In the following, we first describe the methodology for identifying discrete unstable modes, then show the nonlinear evolution of the discrete modes in two scenarios. One scenario has a resonant wave triad, and the other has no resonant wave triad. Results for different scenarios are also discussed in terms of energetics.

a. Linear growth rates

To single out a discrete unstable mode, we first examine the linear growth rates calculated based on Eq. (5) for the specified boundary current using the initial value

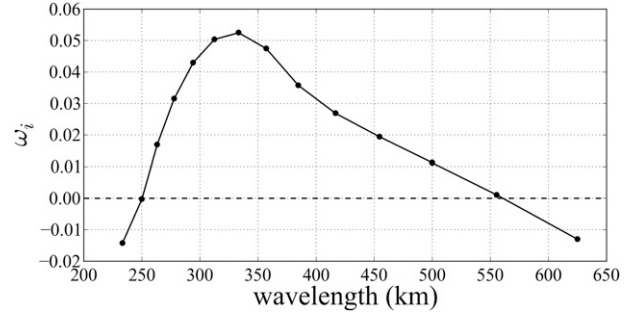


FIG. 3. Linear growth rates normalized by V/L_b as a function of meridional wavelength. The growth rates are calculated by fitting the time series of the integrated perturbation kinetic energy to exponential curves, $EKE = Ce^{2\omega_i t}$, where $\omega_i = lc_i$ is growth rate.

method with friction considered. This calculation uses $\beta = 1.8 \times 10^{-11} (\text{m s})^{-1}$, $L_x = L_y = 5000 \text{ km}$, and $N_x = N_y = 256$. The resulting spatial resolution 19.53 km is sufficient for the most unstable mode, which has a meridional wavelength about 350 km .

The model is initialized with an infinitesimal sine wave in y with a discrete wavenumber $\ell_n = 2n\pi/L_y$, where n is an integer varying from 8 to 20. The corresponding wavelengths $\lambda_n = 2\pi/\ell_n$ range from 625 to 250 km given $L_y = 5000 \text{ km}$.

Figure 3 shows the growth rate as a function of meridional wavelength. There are longwave and short-wave cutoffs at wavelength about 550 and 250 km , respectively. The resolved most unstable mode has wavelength about 350 km . According to the calculation in Fig. 1b, the critical wavenumber dividing the radiating and trapped modes is $l = 0.46$ for the modified sinuous mode and $l = 0.74$ for the modified varicose mode, corresponding to two critical wavelengths $\lambda = 683$ and $\lambda = 425 \text{ km}$, respectively. As a result, modes with a wavelength smaller than 425 km are trapped ones and those with a wavelength larger than 683 km are able to radiate. This is true for both modified varicose and sinuous modes.

b. Case 1, nonlinear resonance

In this experiment, we use the same set of parameters as those used in section 4a, but with $L_y = 700 \text{ km}$ and $N_y = 32$ (the spatial resolution is reduced to 21.88 km from 19.53 km). We can pick a limited number of unstable modes by reducing spectral resolution $2\pi/L_y$ because instabilities are confined in a narrow range of wavelength from 250 to 550 km . Given $L_y = 700 \text{ km}$, the longest mode resolved in the model has a wavelength $\lambda_1 = 700 \text{ km}$. The second and third modes have wavelength $\lambda_2 = 350$ and $\lambda_3 = 233 \text{ km}$, respectively. The

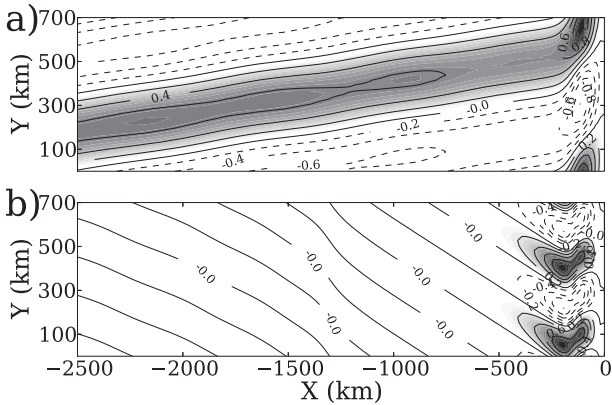


FIG. 4. Streamfunctions at an arbitrary time corresponding to ψ_1 with $\lambda_1 = 700$ km and ψ_2 with $\lambda_2 = 350$ km. They are normalized by their maximum value as they are linear modes. Only the subdomain from $x = -2500$ km to 0 is plotted to show a clearer streamfunction structure.

growth rate curve in Figure 3 shows that only the second mode $n = 2$ has a positive growth rate. In the following, we set the model to support only one unstable mode, and test the two proposed scenarios. Hereafter we refer the mode with wavenumber $\ell_n = 2n\pi/L_y$ as M_n .

Figure 4 shows the streamfunction of M_1 ($\lambda_1 = 700$ km) and M_2 ($\lambda_2 = 350$ km). Here, M_1 is a radiating mode with a streamfunction that decays very slowly westward. The shorter wave mode M_2 , however, is trapped around the boundary current region.

The frequencies for the first four modes are listed in Table 1. It is clear that $\omega_2 + 2\omega_1 = 0$, meaning the frequency relationship between M_1 and M_2 satisfies the requirement for resonance. We also notice that the frequencies of $M_{2,3,4}$ are negative, corresponding to negative phase speed. The longer mode M_1 , however, has a positive frequency (equivalently a positive phase speed), indicating it is a retrograde mode.

Here, M_1 and M_2 satisfy the nonlinear resonance criteria as $\ell_2 = 2\ell_1$ and $\omega_2 + 2\omega_1 = 0$. We now initialize the nonlinear model with random noise, and integrate it in time. Different linear modes can interact and the resonance between M_1 and M_2 is expected.

Figure 5 shows an example of the time series of the perturbation streamfunction at a fixed station in the boundary region and two snapshots of perturbation streamfunction at two developing stages. Three different developing stages are clearly distinguishable in the time series. The amplitude of the streamfunction over stage I ($t = 0 \dots 4.5$ nondimensionalized by $2\pi/\omega_i$) is negligible compared to the finite amplitude at later time. After a period of exponential growth, the second stage

TABLE 1. Frequencies and growth rates of the first four modes.

Mode index	λ (km)	ω_r (cpy)	ω_i (cpy)
1	700	1.44	-0.1554
2	350	-2.88	0.2630
3	233	-6.48	-0.1555
4	175	-10.08	-1.1945

(stage II) is reached and sustained between about $t = 4.5$ and $t = 38$. There is another apparent transition period around $t = 38$, after which perturbations reach the third stage (stage III) with a stronger oscillation.

One should notice that distinguishable stages result from the weakness of the forcing and the slow development of the instability. The forcing scale and the model spectral resolution are reduced to such a level that the model supports only one unstable mode. The slow development of the instability allows for the clear illustration of the physical processes. The system will reach equilibrium significantly faster if the forcing scale or the spectral resolution is increased for the system to support larger growth rates or more than one unstable mode. In a test experiment (not shown) a 9% increase in the amplitude of the basic state shortens the time scale for the emergence of stage II to 0.6 from the original 4.5.

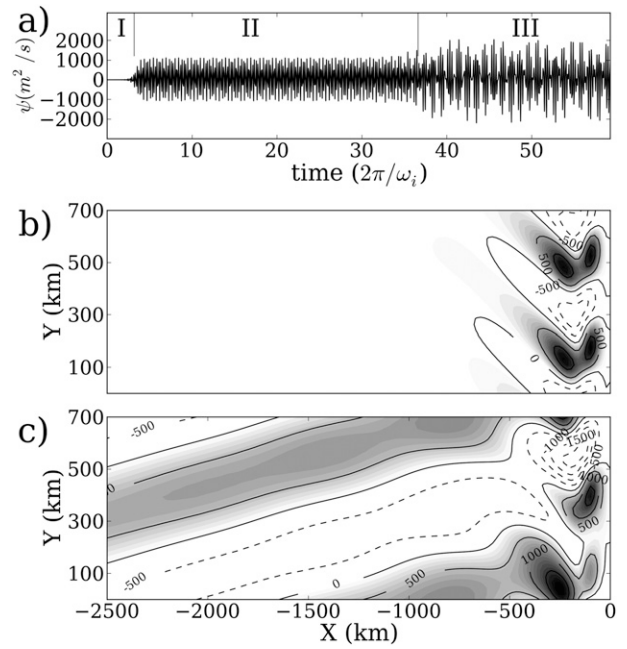


FIG. 5. (a) The time series of the streamfunction at a fixed station in the boundary region. The time axis is nondimensionalized by $2\pi/\omega_i$ in which ω_i of M_2 is chosen. The streamfunction snapshots at (b) $t = 20$ and (c) $t = 50$ are shown. Numerals I, II and III indicate different stages. Unit $\text{m}^2 \text{s}^{-1}$ is used in all panels.

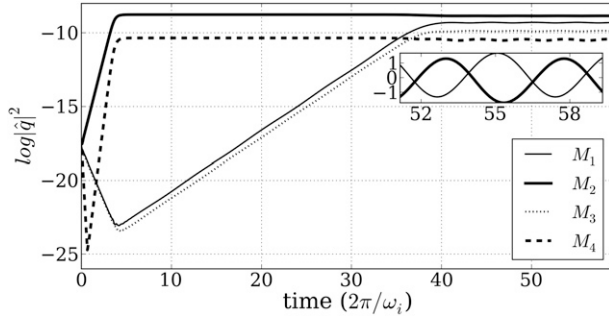


FIG. 6. The time evolution of the enstrophy (s^{-2} in log scale) for the first four modes, $M_{1,2,3,4}$. The minipanel shows the normalized $M_{1,2}$ for $t > 52$.

Two snapshots of the perturbation streamfunction explain the different stages shown in the time series. During stage II, only M_2 is energetically significant. The existence of M_1 with energy extending into the interior is not evident in stage II but clearly shown in stage III (Fig. 5c).

To identify the mechanism that governs the nonlinear perturbation development, we study the time evolution of enstrophy for each mode. The Fourier coefficients for each mode are saved at each time step. The enstrophy for each discretized mode is $|\hat{q}(n, t)|^2$, where \hat{q} is the complex Fourier coefficient of vorticity, n represents the mode index, and t represents time. The time series of the enstrophy for each mode is shown in Fig. 6.

The initial linear development for each mode can be clearly observed in the time series of enstrophy because the parameters used in the integration produce small linear growth rates. Before $t = 0.7$, M_2 (solid line) is the only growing mode, which is expected from the linear study. It grows fastest and reaches nonlinear equilibrium at about $t = 4.5$.

The growth of M_4 (dashed line) after the initial period of decay is caused by the self interaction of M_2 as M_4 is the superharmonic of M_2 in terms of wavenumber. This is essentially a special case of the triad interaction described in Phillips (1960). However, M_4 is only a forced mode by M_2 without resonance because their frequencies do not satisfy the resonance relation. The initial decay of M_4 indicates the initial adjustment of the model to the random noise initialization.

The time series of M_1 and M_3 are similar, but different from those of M_2 and M_4 . Here, M_1 and M_3 decay for $t < 4.5$ with approximately the same negative growth rate, which is consistent with the linear result shown in Fig. 3. They, however, start to grow at $t = 4.5$, when M_2 reaches equilibrium. Linearly decaying modes become nonlinearly unstable, and the linearly unstable mode is eventually equilibrated by nonlinear interaction and friction.

The growths of M_1 and M_3 are obviously caused by their nonlinear interactions with M_2 . The nonlinear interaction between M_2 and M_1 is what we expected as their wavenumbers and frequencies satisfy the nonlinear resonance relation (refer to Table 1). Here, M_1 starts to be resonant with the primary wave M_2 , after M_2 obtains finite amplitude and equilibrates when the energy input from the background mean jet balances the energy loss to dissipation and radiation (quantified in the next section). The growth of M_3 is caused by the interaction between M_1 and M_2 without resonance. During the nonlinear growth, M_1 and M_3 have amplitudes that are too small to feed back into the primary wave M_2 . The nonlinear growth rates of M_1 and M_3 stay constant, until they reach nonnegligible amplitudes around $t = 38$.

The fact that M_1 does not grow from the start but from $t = 4.5$ indicates an important parameter restriction regarding the resonant interaction in the weakly nonlinear regime. For there to be a resonant interaction, the growth rate of M_2 and the decay rate of M_1 must be small. Mathematically, the growth rates of the unstable modes have to be small to define fast and slow time scales as done in Pedlosky (1970); intuitively, the growth of each mode should be slower than its oscillation for a wave triad to have enough time to interact and exchange energy before their amplitudes grow or decay significantly. This condition is violated by the fast growth of M_2 during $t < 4.5$ (Table 1) resulting in a nonresonance condition between M_1 and M_2 . Instead, the resonance starts after M_2 stops growing at $t = 4.5$. M_1 starts to grow because the energy gain of M_1 through nonlinear energy transfer overcomes the energy loss by the direct action of friction.

In the final equilibrium after $t = 38$, the whole system reaches a new balance in which the main players are M_2 and M_1 ; M_3 and M_4 are several orders of magnitude smaller than the two main modes because they are passively forced modes. As the model is weakly forced, the final state is still weakly nonlinear and the interaction between M_1 and M_2 is still clear. Otherwise, resonance loses its meaning in a very nonlinear regime as resonant interaction is no longer a privileged interaction over others.

In summary, there is one primary wave, M_2 , growing linearly during the initial adjustment period. A secondary instability occurs after the primary linear instability reaches a nonlinear equilibrium and is driven by the nonlinear resonance between the primary wave M_2 and the secondary wave M_1 . In the particular circumstance in this study, the secondary wave is the subharmonic of the primary wave. The instability between two harmonics is often referred to as subharmonic instability, which is well studied in the context of internal

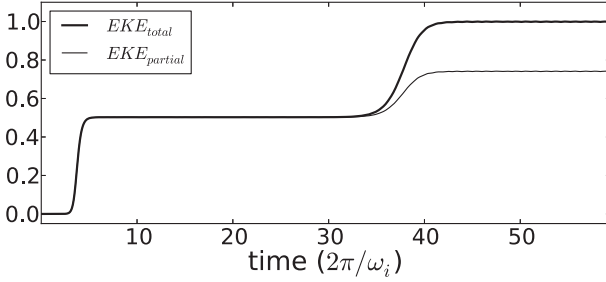


FIG. 7. The perturbation kinetic energy integrated over the whole domain (thick line) and 1000-km-wide eastern boundary domain (thin line) both normalized by EKE_{total} . The discrepancy between these two lines implies the influence of the radiating mode.

gravity waves (McComas and Bretherton 1977, e.g.), but not for barotropic shear instability of meridional currents. Nonlinear self interaction of M_2 and the triad interaction that involves M_1 and M_2 also produce growth for other modes with larger wavenumbers, for example, M_3 and M_4 . Their amplitudes, however, are smaller than M_1 and M_2 .

The cause of the three stages observed in the time series of perturbation streamfunction (Fig. 5a) is clear in the time evolution of the enstrophy for individual modes. During stage I, the primary wave M_2 grows exponentially to gain finite amplitude. During stage II, M_2 stops growing and starts to generate the secondary instability resulting in the growth of M_1 . During stage III, system reaches equilibrium with two energetic modes, M_1 and M_2 .

c. Energetics

The processes mentioned in the previous section can be additionally illuminated by diagnosing the energy budgets of the whole system and each normal mode.

Figure 7 shows the time series of the perturbation kinetic energy integrated over the whole domain (thick line) and over the eastern boundary domain (thin line). During the first two stages, the radiating M_1 is negligible, so that the energy is trapped close to the instability origin around the eastern boundary current. During stage III, the total perturbation energy increases, which is indicated in the time series of the streamfunction at a fixed station (Fig. 5a); the linearly stable but nonlinearly unstable long radiating mode M_1 becomes energetic and sheds a significant amount of energy from the unstable region to the quiescent interior, which is dissipated at the western boundary.

The energy flow can be scrutinized by explicitly calculating the energy budget for each mode. For a truncated model, we can write the vorticity and streamfunction as

$$\begin{aligned} \psi &= \sum_{n=-N_y/2}^{N_y/2} \psi_n = \sum_{n=-N_y/2}^{N_y/2} \phi_n(x, t) \exp(in\ell y) \quad \text{and} \\ q &= \sum_{n=-N_y/2}^{N_y/2} q_n = \sum_{n=-N_y/2}^{N_y/2} \zeta_n(x, t) \exp(in\ell y), \end{aligned} \quad (14)$$

where $\phi_n = \phi_{-n}^*$ to make the variable ψ and q real (the asterisk represents complex conjugate), the ℓ represents the wavenumber of the longest model-resolved wave defined as $\ell = 2\pi/L_y$, and $\zeta_n = (\partial_{xx} - n^2\ell^2)\phi_n$. The linear Jacobians in Eq. (4) become

$$\begin{aligned} J(\psi, \nabla^2 \bar{\psi} + \beta y) + J(\bar{\psi}, \nabla^2 \psi) \\ = \sum_{n=-N_y/2}^{N_y/2} \left[i n \ell \left(\bar{v} \zeta_n - \frac{\partial^2 \bar{v}}{\partial x^2} \phi_n \right) + \beta \frac{\partial \phi_n}{\partial x} \right] e^{in\ell y}. \end{aligned} \quad (15)$$

The discretized Jacobian for perturbations becomes

$$J(\psi, q) = \sum_{m=-N_y/2}^{m=N_y/2} \sum_{j=-N_y/2}^{j=N_y/2} \left(ij\ell \frac{\partial \phi_m}{\partial x} \zeta_j - im\ell \phi_m \frac{\partial \zeta_j}{\partial x} \right) e^{i(j+m)\ell y}. \quad (16)$$

The terms with $j + m = n$ will act as new forcings to the n th mode ψ_n . As a result, Eq. (16) can be rewritten as

$$\begin{aligned} J(\psi, q) &= \sum_{n=-N_y/2}^{N_y/2} J_n \exp(in\ell y) \quad \text{and} \\ J_n &= \sum_{m=-N_y/2}^{N_y/2} ij\ell \left[(n-m) \frac{\partial \phi_m}{\partial x} \zeta_{n-m} - m \phi_m \frac{\partial \zeta_{n-m}}{\partial x} \right], \end{aligned} \quad (17)$$

where $J_n \exp(in\ell y)$ represents the new forcing on the n th mode by nonlinear interaction. For example, for a truncated model with only mode $n = 0, \pm 1, \pm 2$, the nonlinear term for each mode becomes

$$J_0 = i\ell \frac{\partial}{\partial x} (\phi_1^* \zeta_1 - \phi_1 \zeta_1^*) + i2\ell \frac{\partial}{\partial x} (\phi_2^* \zeta_2 - \phi_2 \zeta_2^*), \quad (18)$$

$$\begin{aligned} J_1 &= i\ell \left(\frac{\partial \phi_0}{\partial x} \zeta_1 - \phi_1 \frac{\partial \zeta_0}{\partial x} \right) + i\ell \left(2 \frac{\partial \phi_1^*}{\partial x} \zeta_2 + \phi_1^* \frac{\partial \zeta_2}{\partial x} \right. \\ &\quad \left. - \frac{\partial \phi_2}{\partial x} \zeta_1^* - 2\phi_2 \frac{\partial \zeta_1^*}{\partial x} \right), \quad \text{and} \end{aligned} \quad (19)$$

$$J_2 = i2\ell \left(\frac{\partial \phi_0}{\partial x} \zeta_2 - \phi_2 \frac{\partial \zeta_0}{\partial x} \right) + i\ell \left(\frac{\partial \phi_1}{\partial x} \zeta_1 - \phi_1 \frac{\partial \zeta_1}{\partial x} \right). \quad (20)$$

The terms in J_0 represent the feedback of the perturbations on the basic state. The terms in the first set of

TABLE 2. The kinetic energy budgets integrated over the eastern boundary current region ($-1000 \text{ km} < x < 0$) at different stages. All values are normalized by the total energy input by Reynolds stress at their own stage. The longwave mode is weak at the first stage, but it becomes significant at the second stage. It consequently alters the route of energy transfer.

Budget terms	Stage II			Stage III		
	Total	$n = 1$	$n = 2$	Total	$n = 1$	$n = 2$
Rey	1	0.0002	0.997	1	0.3	0.7
Fric	-1.0083	-0.0001	-0.98	-0.7750	-0.14	-0.57
Flux	-0.0016	-0.0001	-0.004	-0.2597	-0.25	-0.007
Non	—	10^{-6}	-10^{-6}	—	0.1307	-0.1316

parentheses in J_1 and J_2 represent the interaction of M_1 and M_2 with the basic state, respectively. The terms in the second set of parentheses in J_1 represent the interaction between M_1 and M_2 acting as a new forcing to M_1 . The terms in the second set of parentheses in J_2 indicate that the self-interaction of M_1 imposes a new forcing to M_2 .

After substituting Eqs. (14), (15), and (17), Eq. (4) becomes

$$0 = \underbrace{\int_t -\Re \left[\phi_n^* \frac{\partial^2 \phi_n}{\partial x \partial t} + \frac{\beta}{2} \|\phi_n\|^2 - A_H \left(\phi_n^* \frac{\partial^3 \phi_n}{\partial x^3} - \frac{\partial \phi_n^*}{\partial x} \frac{\partial^2 \phi_n}{\partial x^2} - 2n^2 \ell^2 \phi_n^* \frac{\partial \phi_n}{\partial x} \right) \right]_{x=-L_i}}_{\text{flux}} \\ - \underbrace{\left\langle \Im \left(n \ell \frac{\partial \bar{v}}{\partial x} \phi_n^* \frac{\partial \phi_n}{\partial x} \right) \right\rangle}_{\text{rey}} - \underbrace{A_H \left\langle \left\| \frac{\partial^2 \phi_n}{\partial x^2} \right\|^2 + 2n^2 \ell^2 \left\| \frac{\partial \phi_n}{\partial x} \right\|^2 + n^4 \ell^4 \|\phi_n\|^2 \right\rangle}_{\text{fric}} + \underbrace{\langle \Re(\phi_n^* J_n) \rangle}_{\text{non}}, \quad (23)$$

where $\langle \cdot \rangle = L_y \int_t \int_{-L_i}^0 dx dt$, $\|\phi^2\| = \phi \phi^*$. $[A]_{x=-L_i}$ represents the value of A in the interior, and $\Im(A)$ represents the imaginary part of any complex number A . Here, $L_i = 20L_b$ is used but its specific value does not matter much as long as L_i is large enough to include the boundary region. We use “flux,” “rey,” “fric,” and “non” to represent energy contributions resulting from fluxes, Reynolds stress, friction, and nonlinear transfer, respectively. The nonlinear interactions can lead to a rapid energy redistribution among different modes.

The kinetic energy budgets integrated over the eastern boundary current region for the total field and M_1 and M_2 at different stages are listed in Table 2. We rescale all terms with respect to the total energy input by Reynolds stress at each stage, resulting in the rey term being 1 at both stages. The energy radiation only redistributes energy, but does not contribute to the ultimate energy removal. Friction is the only energy sink in a domain-averaged energy budget.

$$\sum_{n=-N_y/2}^{N_y/2} G_n e^{inly}, \quad (21)$$

where G_n represents the governing equation for the n th mode:

$$\frac{\partial \zeta_n}{\partial t} + J_n + \beta \frac{\partial \phi_n}{\partial x} = in\ell \left(\phi_n \frac{\partial^2 \bar{v}}{\partial x^2} - \bar{v} \zeta_n \right) \\ + A_H \left(\frac{\partial^2 \zeta_n}{\partial x^2} - n^2 \ell^2 \zeta_n \right), \quad (22)$$

where A_H is assumed to be a constant. This assumption simplifies but does not change the perturbation energy equation shown next because A_H mainly act on perturbations with large amplitude and small scales over the boundary current region where A_H is approximately constant.

The energy equation for the n th mode is $(\phi_{-n} G_n + \phi_n G_{-n})/2$. After some algebra (see appendix for details), the energy equation for the n th mode is

At stage II, the only dominate mode M_2 is responsible for 99.7% of the total energy input and for about the same amount of energy that is dissipated. Here, M_1 has negligible contribution either in energy input or loss because of its small amplitude. The nonlinear energy transfer between these two modes is infinitesimal.

At stage III, both M_1 and M_2 play important roles in the energy balance. About 30% of the total energy input is done by M_1 and 70% is done by M_2 . Overall, friction accounts for 77.5% of the energy removal for the boundary region. Most (73.5%) of this 77.5% is due to M_2 . The remaining energy removal (out of the boundary region) is done by radiation, mainly because of the divergent term related to the beta effect $(\partial/\partial x)(\beta/2)\|\psi\|^2$ (not shown). The energy radiation is done by M_1 .

The energy budget for each mode is far from being closed without considering the nonlinear energy transfer between the two modes. More energy is needed for M_1 to be steady. However, the nonlinear energy transfer has

no net contribution to the total energy budget because the energy gain in M_1 corresponds to an equal energy loss in M_2 . The total energy budget is closed within 3.5% of the total energy gain.

The quantity M_1 has a positive contribution to the energy input during stage III. In the linear inviscid calculation, the growth rate of M_1 is positive: $\omega_i = 0.045$ corresponding to $l = 2\pi/(L_y/L_b) = 0.45$ (Fig. 1), which means that M_1 can draw energy from the basic state. In the linear viscous calculation, the growth rate of M_1 becomes negative (Table 1) because the energy loss by friction surpasses the energy gain through Reynolds stress, which is still positive. In the nonlinear simulation, however, the energy gain of M_1 through both nonlinear energy transfer and Reynolds stress surpasses the energy drain by friction to yield a positive growth rate. Once M_1 reaches a finite amplitude, the energy gain of M_1 by the Reynolds stress becomes nonnegligible.

In addition, the characteristics of M_1 can be altered by its nonlinear interaction with M_2 . We test this by an extended experiment, in which the model is truncated to have only the basic state and M_1 , starts from the state at $t = 59.4$ with the same parameters and stops at $t = 63$.

Figure 8 shows the energy of M_1 (Fig. 8a) and the streamfunction of M_1 at $t = 59.4$ (Fig. 8b) and $t = 63$ (Fig. 8c). Since there is no energy support from M_2 , M_1 decays (Fig. 8a), which is qualitatively consistent with the prediction by the linear theory (Fig. 3). The structures of M_1 before (Fig. 8b) and after (Fig. 8c) the truncation are different in terms of both zonal tilt and the detailed structures over the boundary current region. Because of the nonlinear interaction with M_2 , M_1 can alter its structure so that the energy transfer from the mean switches from negative, which is predicted by the linear viscous theory, to positive. This phenomenon is clear in the energy budget in Table 2, where the rey (the energy transfer from the mean by the Reynolds stress) of M_1 is positive and accounts for 30% of the total energy input.

This experiment shows that, in a strict sense, Fourier modes in the weakly nonlinear simulations are slightly different from their linear equivalence. The unstable mode can alter the long, stable mode. The longwave mode at finite amplitude is not sustainable without the support of the shortwave mode through nonlinear wave-wave interaction.

Another nonlinear effect is that the finite amplitude perturbations feed back into the mean [the term J_0 in Eq. (18)] to change the structure of the basic boundary current. The modified boundary current will certainly change the stability properties and yield different eigenmodes. The new eigenmodes do not satisfy the requirement for triad-resonance, so that the two harmonics

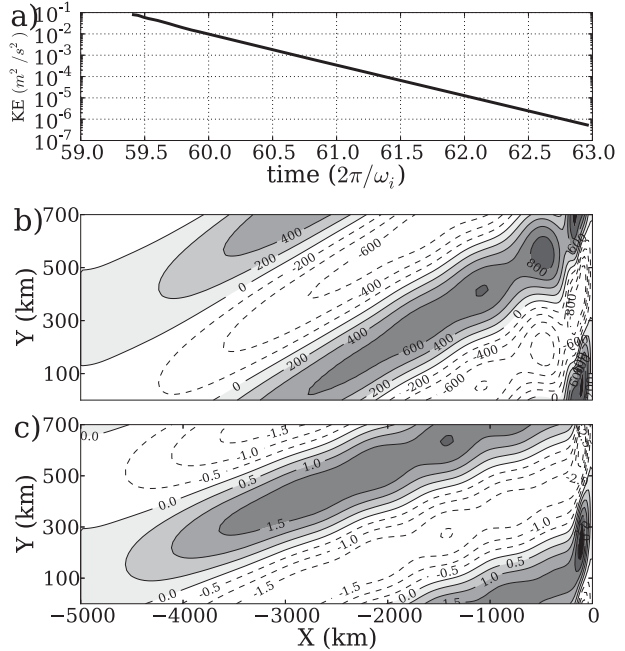


FIG. 8. (a) The time series of the total perturbation kinetic energy ($m^2 s^{-2}$) is shown. The model is truncated to only have the basic state and M_1 . The nonlinear energy transfer from M_2 to M_1 is cutoff by the truncation, M_1 decays in time. This eliminates the possibility of the nonlinear energy transfer from M_2 to M_1 . The streamfunction ($m^2 s^{-1}$) of M_1 at (b) $t = 59.5$ and (c) $t = 63$. Here, M_1 is reconstructed from the total field using Fast Fourier Transform.

decouple, leading to a weaker eddy field. The boundary current will then relax to its unaffected state, generating again the triad resonance to start a new cycle. This mechanism can be detected from the minipanel in Fig. 6 where the energy in different modes oscillates during stage III. The oscillations of M_1 and M_2 are almost out of phase, which can be a sign of changing state of resonance between the two modes. Given less resonance between the two modes, M_1 decays and M_2 grows for the less nonlinear energy transfer from M_2 to M_1 . Similarly, M_1 grows and M_2 decays during more resonance state. This oscillation can be dynamically similar to the finite-amplitude oscillations shown in Pedlosky (1970), however, the detailed study of the oscillation mechanism is beyond the scope of this paper.

We summarize the route of the energy transfer at stage III by the diagram shown in Fig. 9 as follows. The mean boundary jet is supported by an external forcing. It becomes unstable and transfers energy into the eddy field. Here, 70% of this energy goes to the most unstable, trapped mode M_2 , and 30% goes to the long radiating mode M_1 . Of the energy that goes into M_2 , 57% is dissipated locally, and 13% is injected into M_1 through nonlinear energy transfer. The quantity M_1 drains 39%

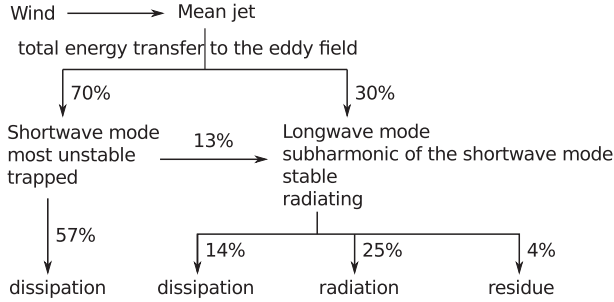


FIG. 9. The schematic diagram showing the route of energy transfer at stage III.

of total energy, of which dissipation accounts for 14% and radiation for 25%. Overall, 57% of the total energy loss is due to the trapped mode and 43% is due to the radiating mode. Although the exact energy partition shown here should not be regarded as an accurate guideline for the eastern boundary currents in the real ocean, this simulation clearly demonstrates that the linearly decaying radiating mode and the most unstable trapped mode become almost equally important in the energy budget for an eastern boundary region.

d. Case 2, nonresonant triad

We keep the same model setup used in the previous section, but we increase β from 1.8×10^{-11} to $2 \times 10^{-11} (\text{m s})^{-1}$. The change of β alters the frequency of the radiating mode M_1 , so that the frequency requirement for nonlinear resonance, $\omega_2 = 2\omega_1$, is not satisfied.

Figure 10 shows the time series of the perturbation streamfunction at a random location in the boundary current (Fig. 10a), a snapshot of the perturbation field in the equilibrium state (Fig. 10b), and the time evolutions of enstrophy for the first four modes (Fig. 10c). The evolution of enstrophy shows that the unstable mode M_2 quickly stands out from the initial random noise and dominates the system after that. Here, M_1 and M_3 decay until their values reach machine precision, and M_4 is sustained by the nonlinear self-interaction of M_2 but with a negligible amplitude.

The frequencies for the first four modes are listed in Table 3, showing a substantial mismatch between ω_2 and $2\omega_1$. As a result, the resonance criterion is not satisfied, and no significant nonlinear interaction happens between these two modes.

The energy budget for this case is similar to the stage II in the previous case, so is not repeated here.

5. Conclusions and discussion

The energy radiation from swift oceanic currents can potentially contribute to the energy in the ocean interior.

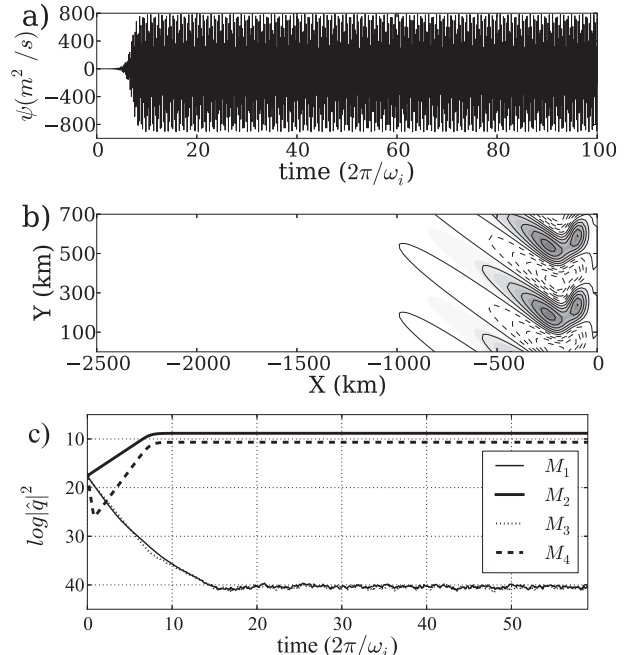


FIG. 10. (a) The time series of the streamfunction ($\text{m}^2 \text{s}^{-1}$) at a random location inside the boundary current, (b) a snapshot of the perturbation streamfunction with a contour interval of $200 \text{ m}^2 \text{s}^{-1}$ at $t = 40$, and (c) the time evolution of the enstrophy (s^{-2} in log scale) of the first four modes.

The orientation of the currents plays an important role in the radiating capability of the instabilities generated by unstable currents. Motivated by previous studies, we investigated the nonlinear radiating instability of a barotropic eastern boundary current.

It is found that the linearly decaying and radiating modes can resonate with an unstable trapped mode to become nonlinearly unstable. These long radiating waves play an important role in the energy budget of an eastern boundary current, as well as in exporting energy into the ocean interior. In our experiment, 25% of total energy gained by instabilities is radiated into the ocean interior.

In our specific model setup, the nonlinear process is related to subharmonic instability, which is caused by the nonlinear resonance between two harmonics. We identify this process by reducing model spectral resolution to single out one unstable mode, then by varying the nondimensional beta to look for wave triad that is

TABLE 3. Frequencies and wavenumbers for the first four modes (case 2). No resonant wave triad exists.

Mode index	λ (km)	ω_r (cpy)
1	700	2.16
2	350	-2.88
3	233	-6.48
4	175	-10.08

resonant. A nonresonant case is also presented as a comparison.

It is noteworthy that the longwave mode is a linearly unstable in an inviscid environment but is suppressed by friction in a viscous environment. It vanishes without nonlinear energy transfer in a viscous setup, as the total energy sink through the radiation and frictional dissipation is greater than its energy gain from the basic state. Its structure is also modified when it nonlinearly interacts with the unstable shortwave mode.

One application of this study is to explain the observed quasi-zonal striations in the ocean interior discovered from satellite altimeter data (Maximenko et al. 2005), some of which extend westward from the eastern boundary. Wang et al. (2012) demonstrated that the nonlinear radiating instabilities of an eastern boundary current can produce zonal striations in the ocean interior with a magnitude that is comparable to the observed values. The interior velocity produced by the radiating instability is about 5 cm s^{-1} , which is comparable to 6.9 cm s^{-1} found in Maximenko et al. (2005) for mid-latitudes ($20^\circ\text{--}40^\circ$). The main point is that even a very idealized eastern boundary current can produce nearly zonal interior flows roughly consistent with observations.

Several phenomena not considered here might also be important for eastern boundary current stability and energy radiation. Baroclinicity can become important and increases the nonlinearity of the system by adding an additional energy source. It is unclear what the characteristics of the radiating baroclinic instabilities are, and whether they obey similar mechanisms so one could extend previous studies of the baroclinic instability of a meridional boundary current by considering a continuous velocity profile with a vertical shear, and also by nonlinear simulations. Furthermore, it is unknown what are the characteristics of the radiating instabilities of a highly nonlinear eastern boundary current with isolated eddies or turbulence embedded.

Eddies and turbulence over the eastern boundary current region may be associated with transient wind forcings. The radiated energy could also come from the inverse cascade of turbulence. If the inverse cascade is a very important process for the energy budget of an eastern boundary current, the beta effect can also become important by radiating the energy of the larger-scale perturbations away from the coastal region. Although it does not destroy energy, the radiation process can drain energy out of a local system. If the energy sink by the radiating instabilities is large, models on an *f*-plane approximation become inappropriate for studies of coastal dynamics.

The baroclinicity in the ocean interior is also important in modifying the radiating instabilities. The Rossby

wave propagation is often constrained by geostrophic contours. In this barotropic study without interior gyres, the geostrophic contours are simply βy . No significantly curved wave rays are evident. However, baroclinic interior gyres associated with sloped isopycnals can modify the PV contours. The instabilities radiated from an eastern boundary current are expected to show different behaviors when they propagate westward depending on their wave characteristics, such as the baroclinic structures. The geostrophic contours in the ocean interior can also be altered by bottom topography, which then influences the wave rays of the radiating instabilities emitted from an eastern boundary current. Furthermore, a sloping bottom topography within the boundary region can also be important in modifying the vertical structure of the boundary current in a baroclinic environment (Spall 2010) and by localizing instabilities.

Acknowledgments. We thank Joe Pedlosky and Hristina Hristova for helpful discussions. The comments from two anonymous reviewers have improved the manuscript greatly. J. Wang would like to thank the rest of his thesis committee Ken Brink and Markus Jochum. J. Wang was supported by the MIT/WHOI education office and the MIT Y-S Fellowship when this study was done, and by NASA Grant NNX12AD47G when this manuscript is prepared. M. Spall is supported by Grant OCE-0926656. G. Flierl is supported by Grant OCE-0752346.

APPENDIX

The Energy Budget for the *n*th Mode

The vorticity equation of the *n*th mode G_n , that is, Eq. (22), is

$$\begin{aligned} & \frac{\partial}{\partial t} \left(\frac{\partial^2 \phi_n}{\partial^2 x} - n^2 \ell^2 \phi_n \right) + J_n + \beta \frac{\partial \phi_n}{\partial x} \\ &= in\ell \left[\phi_n \frac{\partial^2 \bar{v}}{\partial x^2} - \bar{v} \left(\frac{\partial^2 \phi_n}{\partial^2 x} - n^2 \ell^2 \phi_n \right) \right] \\ &+ A_H \left(\frac{\partial^4 \phi_n}{\partial x^4} - 2n^2 \ell^2 \frac{\partial^2 \phi_n}{\partial x^2} + n^4 \ell^4 \phi_n \right). \quad (\text{A1}) \end{aligned}$$

The energy equation can be derived by multiplying ϕ_n^* on both sides of G_n . Note that the energy equation in real space is $0.5(\phi_n^* G_n + \phi_n G_n^*)$, which is equivalent to $0.5(\phi_{-n} G_n + \phi_n G_{-n})$ where ϕ_{-n} is ϕ_n^* and $G_{-n} = G_n^*$. It is also the real part of $\phi^* G_n$ denoted as $\Re(\phi^* G_n)$.

Some terms of $\phi_n^* G_n$ are reorganized as (after dropping the subscript *n* in ϕ_n , and using the subscripts to denote partial derivatives):

$$\begin{aligned}\phi^*(\phi_{xx} - n^2 \ell^2 \phi)_t &= \phi^*(\phi_{xxt} - n^2 \ell^2 \phi_t) = -(\phi_x^* \phi_{xt} + n^2 \ell^2 \phi^* \phi_t) + (\phi^* \phi_{xt})_x, \\ \phi^* inl(\phi \bar{v}_{xx} - \bar{v} \phi_{xx} + n^2 \ell^2 \bar{v} \phi) &= inl \phi^* \phi \bar{v}_{xx} - inl(\bar{v} \phi^* \phi_x)_x + inl \bar{v}_x \phi^* \phi_x + inl \bar{v}(\phi_x^* \phi_x + n^2 \ell^2 \phi^* \phi), \quad \text{and} \\ \phi^* A_H(\phi_{xxxx} - 2n^2 \ell^2 \phi_{xx} + n^4 \ell^4 \phi) &= A_H(\phi^* \phi_{xxx} - \phi_x^* \phi_{xx} - 2n^2 \ell^2 \phi^* \phi_x)_x + A_H(\phi_{xx}^* \phi_{xx} + 2n^2 \ell^2 \phi_x \phi_x^* + n^4 \ell^4 \phi^* \phi).\end{aligned}$$

The energy equation for the n th mode in real space $0.5(\phi_{-n} G_n + \phi_n G_{-n})$ can be written as:

$$\begin{aligned}E_t &= \Re \left[\phi^* \phi_{xt} + \frac{\beta}{2} \|\phi\|^2 + n \ell \bar{v} \phi^* \phi_x - A_H(\phi^* \phi_{xxx} \right. \\ &\quad \left. - \phi_x^* \phi_{xx} - 2n^2 \ell^2 \phi^* \phi_x)_x - \Im(n \ell \bar{v}_x \phi^* \phi_x) \right. \\ &\quad \left. - A_H(\|\phi_{xx}\|^2 + 2n^2 \ell^2 \|\phi_x\|^2 + n^4 \ell^4 \|\phi\|^2) + \Re(\phi^* J_n), \right.\end{aligned}$$

$$0 = \underbrace{\int_t -\Re \left[\phi^* \phi_{xt} + \frac{\beta}{2} \|\phi\|^2 - A_H(\phi^* \phi_{xxx} - \phi_x^* \phi_{xx} - 2n^2 \ell^2 \phi^* \phi_x) \right]_{x=-L_i}}_{\text{flux}} \\ - \underbrace{\langle \Im(n \ell \bar{v}_x \phi^* \phi_x) \rangle}_{\text{rey}} - \underbrace{A_H(\|\phi_{xx}\|^2 + 2n^2 \ell^2 \|\phi_x\|^2 + n^4 \ell^4 \|\phi\|^2)}_{\text{fric}} + \underbrace{\langle \Re(\phi^* J_n) \rangle}_{\text{non}}, \quad (\text{A2})$$

where the boundary conditions: $\phi = 0$ and $\phi_x = 0$ at the side boundary $x = 0$, and $\bar{v} = 0$ in the interior ($L_i = 20L_b$ in this case) are used. We use “flux” to denote the contribution of fluxes by pressure, radiation, and friction, “rey” the effect of Reynolds stress, “fric” the energy dissipation by friction, and “non” the nonlinear energy transfer. After substituting the subscript n for ϕ , the energy budget equation becomes Eq. (23).

The energy equation can be further simplified by dropping the frictional fluxes, which are negligible in the interior comparing with the beta effect because of the

$$0 = \underbrace{\int_t -\Re \left[\phi^* \phi_{xt} + \frac{\beta}{2} \|\phi\|^2 \right]_{x=-L_i}}_{\text{flux}} - \underbrace{\langle \Im(n \ell \bar{v}_x \phi^* \phi_x) \rangle}_{\text{rey}} - \underbrace{A_H(\|\phi_{xx}\|^2 + 2n^2 \ell^2 \|\phi_x\|^2 + n^4 \ell^4 \|\phi\|^2)}_{\text{fric}} + \underbrace{\langle \Re(\phi^* J_n) \rangle}_{\text{non}}. \quad (\text{A3})$$

The energy budget discussed in the text is calculated based on Eq. (A2), but the one based on Eq. (A3) is approximately the same.

REFERENCES

- Brink, K. H., and T. J. Cowles, 1991: The coastal transition zone program. *J. Geophys. Res.*, **96** (C8), 14 637–14 647.

where $E = 1/2(\|\phi_x\|^2 + n^2 \ell^2 \|\phi\|^2)$, $\|\phi^2\| = \phi \phi^*$, and $\Im(A)$ represents the imaginary part of a complex number A .

Taking the time and domain integration over the eastern boundary current region

$$\langle \cdot \rangle = \int_t \int_0^{L_y} \int_{-L_i}^0 \equiv L_y \int_t \int_{-L_i}^0$$

for a meridionally periodic domain, the energy equation then becomes

high-order horizontal derivatives. The parameter measuring the importance of friction is

$$E = \mathcal{O} \left(\frac{A_H/L^3}{\beta} \right),$$

which is $\mathcal{O}(10^{-4})$ given $\beta = 1.8 \times 10^{-11} (\text{m s})^{-1}$, $A_H = 100 (\text{m}^2 \text{s}^{-1})$, and the typical meridional scale of the perturbation field $L = 700 \text{ km}$ in the interior. Here, E becomes even smaller if the interior perturbation zonal scale $L \approx 2000 \text{ km}$ is used. As a result, the frictional fluxes in the interior are negligible, the energy equation then becomes

- Davis, R. E., 1985: Drifter observations of coastal surface current during CODE: The method and descriptive view. *J. Geophys. Res.*, **90** (C3), 4741–4755.

- Fantini, M., and K. K. Tung, 1987: On radiating waves generated from barotropic shear instability of a western boundary current. *J. Phys. Oceanogr.*, **17**, 1304–1308.

- Flierl, G. R., and V. Kamenkovich, 1975: Gulf Stream meandering and Gulf Stream Ring eddy production mechanism. *Dynamics and the Analysis of MODE-1*, A. R. Robinson, Ed., MIT, 250 pp.

- Fox-Kemper, B., 2003: Eddies and friction: Removing of vorticity from the wind-driven gyre. Ph.D. thesis, MIT/WHOI Joint Program in Oceanography, 310 pp.
- Gill, A., J. Green, and A. Simmons, 1974: Energy partition in the large-scale ocean circulation and the production of mid-ocean eddies. *Deep Sea Res. Oceanogr. Abstr.*, **21**, 499–528, doi:10.1016/0011-7471(74)90010-2.
- Harrison, D. E., and A. R. Robinson, 1979: Boundary-forced planetary waves: A simple model midocean response to strong current variability. *J. Phys. Oceanogr.*, **9**, 919–929.
- Hickey, B. M., 1979: The California current system—Hypotheses and facts. *Prog. Oceanogr.*, **8**, 191–279, doi:10.1016/0079-6611(79)90002-8.
- Hristova, H. G., J. Pedlosky, and M. A. Spall, 2008: Radiating instability of a meridional boundary current. *J. Phys. Oceanogr.*, **38**, 2294–2307.
- Kamenkovich, I. V., and J. Pedlosky, 1996: Radiating instability of nonzonal ocean currents. *J. Phys. Oceanogr.*, **26**, 622–643.
- , and —, 1998a: Radiation of energy from nonzonal ocean currents, nonlinear regime. Part I: Single wave development. *J. Phys. Oceanogr.*, **28**, 1683–1701.
- , and —, 1998b: Radiation of energy from nonzonal ocean currents, nonlinear regime. Part II: Interactions between waves. *J. Phys. Oceanogr.*, **28**, 1683–1701.
- Lipps, F., 1962: The barotropic stability of the mean winds in the atmosphere. *J. Fluid Mech.*, **12**, 397–407.
- Malanotte-Rizzoli, P., D. B. Haidvogel, and R. E. Young, 1987: Numerical simulation of transient boundary-forced radiation. I: The linear regime. *J. Phys. Oceanogr.*, **17**, 1439–1457.
- Maximenko, N., B. Bang, and H. Sasaki, 2005: Observational evidence of alternating zonal jets in the world ocean. *Geophys. Res. Lett.*, **32**, L12607, doi:10.1029/2005GL022728.
- McComas, C. H., and F. P. Bretherton, 1977: Resonant interaction of oceanic internal waves. *J. Geophys. Res.*, **82**, 1397–1412.
- Pedlosky, J., 1970: Finite-amplitude baroclinic waves. *J. Atmos. Sci.*, **27**, 15–30.
- , 1975: A note on the amplitude of baroclinic waves in the mid-ocean. *Deep Sea Res. Oceanogr. Abstr.*, **22**, 575–576.
- , 1977: On the radiation of meso-scale energy in the mid-ocean. *Deep-Sea Res.*, **24**, 591–600.
- , 1993: The reflection of unstable baroclinic waves and the production of mean coastal currents. *J. Phys. Oceanogr.*, **23**, 2130–2135.
- Phillips, O. M., 1960: On the dynamics of unsteady gravity waves of finite amplitude. Part 1. The elementary interactions. *J. Fluid Mech.*, **9**, 193–217.
- Robinson, A. R., and J. C. McWilliams, 1974: The baroclinic instability of the open ocean. *J. Phys. Oceanogr.*, **4**, 281–294.
- Spall, M. A., 2000: Generation of strong mesoscale eddies by weak ocean gyres. *J. Mar. Res.*, **58**, 97–116.
- , 2010: Non-local topographic influences on deep convection: An idealized model for the Nordic Seas. *Ocean Modell.*, **32** (1–2), 72–85, doi:10.1016/j.ocemod.2009.10.009.
- Stammer, D., 1997: Global characteristics of ocean variability estimated from regional TOPEX/Poseidon altimeter measurements. *J. Phys. Oceanogr.*, **27**, 1743–1769.
- Talley, L. D., 1983: Radiating barotropic instability. *J. Phys. Oceanogr.*, **13**, 972–987.
- Wang, J., M. A. Spall, G. R. Flierl, and P. Malanotte-Rizzoli, 2012: A new mechanism for the generation of quasi-zonal jets in the ocean. *Geophys. Res. Lett.*, **39**, L10601, doi:10.1029/2012GL051861.
- Wyrki, K., L. Magaard, and J. Hager, 1976: Eddy energy in the oceans. *J. Geophys. Res.*, **81**, 2641–2646.